

THE EVOLVING RELATIONS BETWEEN SIZE, MASS, SURFACE DENSITY, AND STAR FORMATION IN 3×10^4 GALAXIES SINCE $z = 2$

RIK J. WILLIAMS^{1,2}, RYAN F. QUADRI¹, MARIJN FRANX¹, PIETER VAN DOKKUM³, SUNE TOFT^{4,5}, MARISKA KRIEK⁶,
AND IVO LABBÉ^{2,7}

¹ Leiden Observatory, Leiden University, Niels Bohrweg 2, NL-2333 CA Leiden, The Netherlands; williams@obs.carnegiescience.edu

² Carnegie Observatories, Pasadena, CA 91101, USA

³ Department of Astronomy, Yale University, New Haven, CT 06520-8101, USA

⁴ Dark Cosmology Centre, Niels Bohr Institute, University of Copenhagen, Juliane Maries Vej 30, DK-2100 Copenhagen, Denmark

⁵ European Southern Observatory, Karl-Schwarzschild-Str. 2, D-85748 Garching bei München, Germany

⁶ Department of Astrophysical Sciences, Princeton University, Princeton, NJ 08544, USA

Received 2009 June 25; accepted 2010 March 5; published 2010 March 25

ABSTRACT

The presence of massive, compact, quiescent galaxies at $z > 2$ presents a major challenge for theoretical models of galaxy formation and evolution. Using one of the deepest large public near-IR surveys to date, we investigate in detail the correlations between star formation and galaxy structural parameters (size, stellar mass, and surface density) from $z = 2$ to the present. At all redshifts, massive quiescent galaxies (i.e., those with little or no star formation) occupy the extreme high end of the surface density distribution and follow a tight mass–size correlation, while star-forming galaxies show a broad range of both densities and sizes. Conversely, galaxies with the highest surface densities comprise a nearly homogeneous population with little or no ongoing star formation, while less dense galaxies exhibit high star formation rates and varying levels of dust obscuration. Both the sizes and surface densities of quiescent galaxies evolve strongly from $z = 2$ –0; we parameterize this evolution for both populations with simple power-law functions and present best-fit parameters for comparison to future theoretical models. Higher-mass quiescent galaxies undergo faster structural evolution, consistent with previous results. Interestingly, star-forming galaxies’ sizes and densities evolve at rates similar to those of quiescent galaxies. It is therefore possible that the same physical processes drive the structural evolution of both populations, suggesting that “dry mergers” may not be the sole culprit in this size evolution.

Key words: cosmology: observations – galaxies: evolution – galaxies: high-redshift – galaxies: structure

Online-only material: color figures

1. INTRODUCTION

Ample evidence now exists for the presence of massive galaxies at $z > 2$ with little or no ongoing star formation, suggesting that a non-negligible fraction of the local early-type galaxy population was effectively in place only a few Gyr after the big bang, and that massive red galaxies constitute a significant fraction of (or possibly even dominate) the stellar mass density at $z \sim 2$ (e.g., McCarthy et al. 2004; Labbé et al. 2005; Daddi et al. 2005; Kriek et al. 2006, 2008a; Rudnick et al. 2006; Marchesini et al. 2007; Stutz et al. 2008; Toft et al. 2009). Although their masses and star formation rates (SFRs) are nominally similar, it has since become clear that these quiescent galaxies at $z > 1$ have dramatically different structures compared to local ellipticals: specifically, the high-redshift galaxies’ sizes are much smaller (e.g., Daddi et al. 2005; Trujillo et al. 2006a; Zirm et al. 2007; Toft et al. 2007; van Dokkum et al. 2008; Cimatti et al. 2008; Damjanov et al. 2009). Their surface densities likewise evolve strongly with redshift, as does the “threshold” surface density above which galaxies are predominantly quiescent (Franx et al. 2008; Maier et al. 2009). These phenomena pose several new challenges for studies of galaxy formation. Indeed, if massive quiescent galaxies at $z \sim 2$ were almost universally compact and dense, why are similar objects in the local universe practically nonexistent (e.g., Trujillo et al. 2009; Taylor et al. 2009b)?

Several mechanisms for this transformation have been proposed, including a scenario whereby local early-type galaxies are built through a series of “dry” (i.e., gas-poor) mergers of these compact progenitors (Khochfar & Silk 2008; Hopkins et al. 2009b; Feldmann et al. 2009). Such mergers, being largely non-dissipative, would over time tend to “puff up” compact galaxies. Some observational estimates of the major dry merger rate since $z \sim 1$ indicate that these are indeed a factor in the buildup of massive galaxies (Bell et al. 2006; Bundy et al. 2009; de Ravel et al. 2009), but the remnants of such major mergers would also have correspondingly larger masses and so it is unclear whether major dry mergers can entirely solve the size–mass discrepancy (though they are likely to mitigate it to some degree; e.g., van der Wel et al. 2009). Minor mergers may be a more important process—both from a simple virial argument (Naab et al. 2009) and because massive compact “cores” at high redshift may accrete material in their outskirts to form the massive ellipticals seen today (Bezanson et al. 2009; Hopkins et al. 2009a; van Dokkum et al. 2010). However, theoretical models have yet to converge on a definitive explanation—some proposed models predict galaxy sizes dramatically different from those observed (Joung et al. 2009), while others match observed sizes at $z = 2$ and $z = 0$ (Khochfar & Silk 2006) but not at $z \sim 1$ (van der Wel et al. 2008).

Whatever the underlying mechanism may be, observations of large samples of galaxies over a broad redshift range are crucial to adequately test current and upcoming models. However, many of the aforementioned galaxy structure studies employ

⁷ Hubble fellow.

HST–NICMOS, which provides accurate size measurements but can typically image only one target at a time and is thus inadequate for observing very large samples. Optical imagers are much larger, but at $z \sim 2$ near-IR data are more robust for size determinations; these bands fall in the rest-frame optical and therefore better trace the distribution of stellar mass than the rest-frame UV (observed optical). Furthermore, spectroscopy of quiescent galaxies (both to determine their redshifts and confirm their quiescence) requires large amounts of observing time due to the absence of strong emission lines; again, while this can be performed for a few bright galaxies at $z \sim 2$ with current facilities (Kriek et al. 2006), it is infeasible for the large samples of fainter objects needed to provide a comprehensive view of the high-redshift galaxy population.

Fortunately, although spectroscopy and space-based imaging give the most precise picture of star formation and galactic structure for individual objects, the average properties of large samples can be accurately investigated with less “expensive” data. For example, both Trujillo et al. (2006b) and Franx et al. (2008) successfully based their galaxy size measurements on ground-based imaging and photometric redshifts. Although there are inherently greater uncertainties on the size and mass of any individual object than with NICMOS imaging and spectroscopic redshifts, the *average* structural parameters of large populations can be accurately determined. Furthermore, even without spectroscopy there are several ways to determine which galaxies are quiescent and which are actively forming stars. One straightforward method is to identify galaxies on the “red sequence” (using, e.g., the rest-frame $U - V$ color), which at low redshift is primarily composed of quiescent galaxies with strong 4000 Å breaks. However, star-forming galaxies containing large amounts of dust can have similarly red colors, so “red and dead” galaxy samples selected through this color cut are likely to be contaminated with substantial numbers of “red and dusty” starbursts with increasing redshift (e.g., Williams et al. 2009).

With photometric observations in a suitable set of filters, the shape of the broadband spectral energy distribution (SED) can be used to distinguish between the sharp 4000 Å break characteristic of old stellar populations and the more gradual reddening caused by dust absorption; the best-fit SFRs and dust column densities from SED modeling codes can then be used to define quiescent galaxy samples. Empirical selection techniques using multiple rest-frame colors, such as the one employed by Williams et al. (2009), are also effective at separating dusty from “dead” galaxies up to $z = 2$ (and even higher; I. Labbé et al. 2010, in preparation) with little dependence on input templates or models. Coupled with the large, deep multiwavelength surveys and improved photometric redshift techniques that have emerged in the past few years, these diagnostics provide an unprecedented view of star formation and its relation to other physical properties in massive galaxy populations.

Using the largest such publicly available data set with sufficient depth, the UKIDSS Ultra-Deep Survey (UDS; and overlapping imaging from the Subaru–*XMM* Deep Survey (SXDS) and *Spitzer* Wide-Area Extragalactic Survey (SWIRE)), we analyze the structural evolution of quiescent galaxies up to $z = 2$, specifically the correlations between star formation activity, galaxy size, and stellar mass surface density. First, in Section 2 we review the data and describe the size and mass measurements employed for this study. Next in Section 3, we investigate how the specific star formation rate (sSFR) is related to galaxy mass, size, and surface density, and in Section 4 present

quantitative constraints on the evolution of these structural properties for both star-forming and quiescent galaxies. Finally, the uniformity of the connections between star formation and structure is discussed in Section 5 along with some novel ways to interpret these correlations. AB magnitudes and a concordance cosmology ($h = 0.7$, $\Omega_M = 0.3$, $\Omega_\Lambda = 0.7$) are assumed throughout.

2. DATA AND MEASUREMENTS

The high-redshift galaxy sample analyzed herein is based on an updated version of the K -selected galaxy catalog⁸ described in detail by Williams et al. (2009); a brief summary follows. This catalog comprises near-infrared J and K data taken from the UKIDSS UDS Data Release 1 (Lawrence et al. 2007; Warren et al. 2007), with overlapping $BRi'z'$ imaging from the SXDS (Sekiguchi et al. 2004), and 3.6/4.5 μm data from the SWIRE survey (Lonsdale et al. 2003). Using the positions and shapes of bright but unsaturated stars in the different bands, all mosaics were astrometrically matched and convolved to consistent point-spread functions (PSFs). Using the SExtractor software (Bertin & Arnouts 1996), “color” fluxes were measured in fixed $1''.75$ apertures and total K fluxes from flexible elliptical (Kron 1980) apertures.

In addition to the original Williams et al. (2009) catalog, we incorporate the H -band mosaic from the UKIDSS Data Release 3 (to be described by S. J. Warren et al. 2010, in preparation) with PSF and astrometric matching and flux measurements performed in the same manner as with the other bands. Photometric redshifts were calculated with the H data included using the publicly available code EAZY (Brammer et al. 2008). The new photometric redshifts differed very little from the original ones presented by Williams et al. (2009), but inclusion of the H band should in principle improve both the z_{phot} values and stellar mass estimates at $z \gtrsim 2$. At the adopted flux limit of $K < 22.4$, this catalog contains nearly 3×10^4 galaxies.

Because of its depth and $\sim 0.8 \text{ deg}^2$ area, the UDS is well suited for studies of large galaxy samples at $z \gtrsim 0.5$; at lower redshifts, however, the comoving volume probed by the UDS is too small to provide meaningful samples (and may also be severely affected by cosmic variance). Thus, for comparison to the UDS we also include the same $z \sim 0.06$ SDSS sample used by Franx et al. (2008). To summarize, this sample was originally defined by Kauffmann et al. (2003), and Franx et al. (2008) performed minor corrections in the mass-to-light ratios (accounting for the fact that the galaxy centers, where the spectroscopic fibers are placed, are typically redder than the outskirts) as well as total flux corrections. The redshift range of $z = 0.05\text{--}0.07$ was chosen to avoid selection effects on galaxies with high mass (at the low- z end) and small angular sizes (at higher redshift).

2.1. Sizes

2.1.1. Fitting

Size measurements were performed in a manner similar to that by Toft et al. (2007). We use the Galfit software package (Peng et al. 2002) to fit Sérsic (1968) models to all bright ($K < 22.4$) sources detected in the unconvolved (i.e., before PSF matching, to ensure the highest possible angular resolution) UDS K image. This image had a typical seeing FWHM of $0''.7$.

⁸ Available from <http://www.strw.leidenuniv.nl/galaxyevolution/UDS>.

First a square postage stamp 21 pixels ($4''.2$) on a side was made around each galaxy to be fitted. Initial guesses for the effective radius r_e , magnitude, ellipticity, and position angle were taken from the SExtractor catalog. The PSF used by Galfit to deconvolve the galaxy images is the average PSF over the image (taken as the median of 300 bright, unsaturated stars; also used in the PSF-matching step described in Williams et al. 2009). The Sérsic parameter n was allowed to vary between 1 and 4, and the effective radius between $0''.01$ (effectively a point source) and $15''$. Since galaxies in general may exhibit color gradients, it is important to measure sizes at approximately the same rest-frame wavelength when comparing samples at different redshifts. The procedure described above was thus repeated for the unconvolved J and H images (both exhibiting $0''.8$ seeing), and we define the size of a galaxy as its circularized effective radius ($r_e = \sqrt{ab}$) at a rest-frame wavelength of 8000 \AA , interpolated from the size measurements of the two adjacent bands. In other words, when rest-frame 8000 \AA falls between two observed bands i and j , the interpolated size is

$$r_{e,8000} = r_{e,i} + \frac{r_{e,j} - r_{e,i}}{\lambda_j - \lambda_i} [8000 \text{ \AA}(1+z) - \lambda_i]. \quad (1)$$

In practice, the interpolated sizes are quite similar to those computed by, e.g., simply taking the size measured from the observed band closest to 8000 \AA . However, the interpolation method smoothes out possible discretization effects due to the choice of the measurement filter and also in principle helps to mitigate failed size measurements in a given band.

2.1.2. Simulations

Previous studies have shown that reliable galaxy sizes can be measured from ground-based data, provided the signal-to-noise ratio is sufficiently high and the PSF across the image is stable (e.g., Trujillo et al. 2006b; Franx et al. 2008). For instance, Trujillo et al. (2006b) use simulations to investigate systematic effects, finding them to be minimal down to $r_e \sim (0.2\text{--}0.3) \times \text{FWHM}(\text{PSF})$, though individual measurements exhibit a large degree of scatter. The effective radius is typically the most robust structural parameter measured; other variables defining the profile shape (e.g., Sérsic index and axis ratio) are far more susceptible to systematic uncertainties.

It is nonetheless instructive to investigate whether the specific characteristics of the UDS data and our fitting techniques have introduced systematic biases; we thus performed simulations analogous to Trujillo et al. (2006b) to test our effective radius measurements. Model galaxy profiles over a range of magnitudes $K = 18\text{--}23$, r_e from 0.1 to 1 arcsec, and $n = 1\text{--}4$ were created; these were chosen to span typical galaxy angular sizes at $z = 1\text{--}2$. Blank postage stamps (containing only noise) were then cut from random positions in the UDS K -band image and the model galaxies added to them. The identical fitting procedure used on the real images was then applied to 15,000 such simulated postage stamps to derive the output effective radii.

Figure 1 shows the distribution of input and output effective radii, and the fractional difference between the two, as a function of input effective radius. Brighter galaxies are plotted as larger points. As expected, relatively faint galaxies exhibit larger random uncertainties in their size measurements. While systematic deviations are seen for both the faintest and largest galaxies, these are relatively small (with a median of $\sim 10\%$) compared to the random errors; additionally, since we only include galaxies with $z > 0.5$ in our analysis, objects with

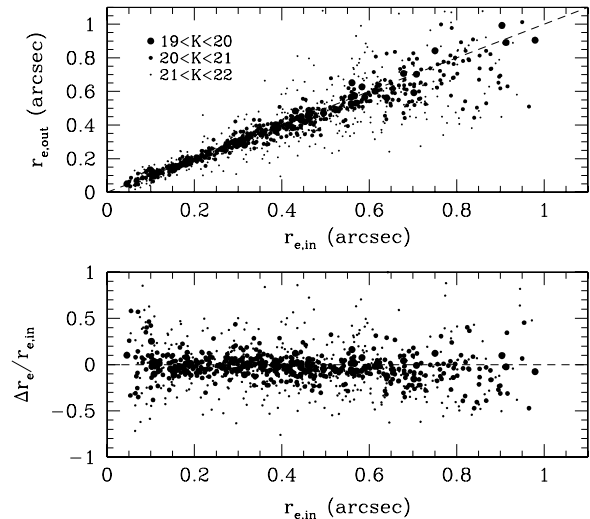


Figure 1. Top panel: output effective radii of simulated galaxies as a function of $r_{e,\text{in}}$. Larger point sizes represent brighter galaxies; for clarity only a random 10% of our simulated galaxies in these magnitude bins are plotted. Bottom panel: fractional deviation $(r_{e,\text{out}} - r_{e,\text{in}})/r_{e,\text{in}}$ as a function of input radius. Fainter galaxies exhibit larger random uncertainties. Although the faintest, largest galaxies show a small systematic offset (10%–20% at worst), these deviations are small compared to the random scatter and the measured trends with redshift discussed in Section 4.

such large angular sizes are quite rare. These observed offsets are comparable to the offsets reported by Trujillo et al. (2006b); most importantly, the average effective radii of galaxies with sizes $\sim 0''.1\text{--}1''.0$ appear to be reasonably reliably recovered. Given the large scatter, however, it should be noted that individual measurements of galaxy sizes are highly uncertain even if ensemble averages are accurate.

2.1.3. Empirical Consistency Tests

The simulations described above provide a realistic view of some of the random and systematic uncertainties in this analysis. However, to some extent these are idealized; for example, the evident ability to measure effective radii as small as one-half of a pixel may be true in a numerical sense, but in real images additional effects such as PSF variations will limit the precision that can be achieved. We therefore supplement the simulations with a set of purely empirical tests to better assess the reliability of the galaxy size measurements. Specifically, we check the following three important assumptions: (1) the simple interpolation of galaxy sizes between different bands is robust; (2) a single PSF is sufficient to model the entire image; and (3) the fitting box size of $4''.2$ is large enough to obtain reasonable fits.

First, to test the interpolation assumption, we estimated the H -band sizes by averaging the measured J and K sizes; the estimated and measured H sizes matched very well with no noticeable systematic offset. The “single PSF” assumption (2) was tested by generating four different PSFs, each composed of bright stars from the four quadrants of the K mosaic, and re-measuring the sizes of galaxies within the central $40'' \times 40''$ of the K mosaic. While there were small systematic differences in the sizes measured with the different PSFs, these were on the order of $0''.02$, which is effectively negligible compared to typical measured galaxy sizes of $0''.2\text{--}1''.0$. Similarly, the median galaxy sizes show no evidence of systematic deviations with position in the image, indicating that the PSF does not significantly vary. Finally, the box-size assumption (3) was tested by re-fitting a

subset of galaxies using postage stamp sizes of $5''.2$ and $6''.2$; the new sizes were fully consistent with those measured in the original $4''.2$ cutouts. The exception to this is the largest objects in this sample with $r_e \gtrsim 1''.2$ (about 10 kpc radius at $z = 1-2$); these objects exhibit 30% larger sizes when a larger fitting box is used, but such objects comprise only a tiny fraction ($<4\%$) of our $z > 0.5$ sample and so do not affect our results.

Re-fitting the same subset of galaxies using different PSFs and box sizes also gives an estimate of the measurement uncertainties (i.e., the degree to which a given size measurement is reproducible given different assumed input parameters). Between $0''.2$ and $1''.0$ the measured sizes were consistent with each other within $\sim 5\%$; at $0''.1$ the fractional error rapidly increases to about 10%–15%, and at smaller effective radii sizes can no longer be reliably inferred. To determine the efficiency to which Galfit can distinguish between point sources and extended objects in these data, we also measured the radii of stars (found via color selection) using the same fitting parameters. Interestingly, while essentially all of the stars have best-fit radii of zero (as is expected for point sources), Galfit measures non-zero radii for the vast majority of compact galaxies—even those with best-fit radii much smaller than the PSF.

Thus, these simulations and empirical tests confirm that effective radius measurements are likely free of major systematic effects down to $r_e = 0''.1-0''.2$. Even if some offsets are present (as seen in our simulations and those by Trujillo et al. 2006b), they are comparable to or smaller than the systematic uncertainties on other parameters (e.g., in mass, redshift, and SFR determinations). We therefore conclude that measurements of the average sizes of large galaxy samples down to small radii are robust given these data. This is similar to what Franx et al. (2008) found by fitting their ground-based data and comparing it to Advanced Camera for Surveys (ACS) imaging.

2.2. Stellar Masses and Star Formation Rates

The stellar masses of galaxies in this sample were calculated with the *Fitting and Assessment of Synthetic Templates* (FAST) code (Kriek et al. 2009). This code uses χ^2 minimization to fit Bruzual & Charlot (2003) stellar population evolution models to the observed broadband photometry. A Salpeter (1955) initial mass function (IMF) and solar metallicity were assumed; masses were then shifted by a factor of -0.2 dex for consistency with the $z \sim 0$ Sloan Digital Sky Survey (SDSS) masses (which were computed with a Kroupa 2001 IMF). We re-fitted a subset with Maraston (2005) models and both IMFs to verify that this factor is essentially constant and does not vary systematically with galaxy color or mass. Redshifts were fixed to the z_{phot} values derived by EAZY, and a variety of evolutionary histories were allowed in the fitting, including exponentially declining ($\text{SFR} \sim e^{-t/\tau}$) models with τ ranging from 10^7-10^{10} Gyr. The computed masses are consistent with those calculated using other standard methods, for example, using HYPERZ as a fitting engine and scaling the model amplitudes to estimate masses (as done by, e.g., Förster Schreiber et al. 2004). Note that Maraston (2005) models result in galaxy masses approximately 0.2 dex lower than Bruzual & Charlot (2003) models; however, unlike the IMF correction factor, this discrepancy varies somewhat with galaxy mass.

Other parameters, such as the degree of dust extinction A_V , average stellar population ages, exponential factor τ , and SFR are also computed by FAST during the SED fitting procedure. Most of these are highly uncertain when based on broadband data (Kriek et al. 2008b); however, the *sSFR* ($s\text{SFR} = \text{SFR}/M_*$)

is somewhat more robust. This quantity, taking the mass of the host galaxy into account, provides a more meaningful characterization of star formation activity (e.g., an SFR of $10 M_\odot \text{ yr}^{-1}$ is far more significant in a dwarf galaxy than a giant elliptical). Furthermore, since the total SFR and mass both exhibit a similar dependence on the assumed IMF, the *sSFR* is less sensitive to the choice of IMF and input stellar population model(s) than the absolute SFR.

2.3. Rest-frame Fluxes

Rest-frame colors, particularly the combination of $U - V$ and $V - J$, are invaluable for distinguishing quiescent galaxies from those actively forming stars (Wuyts et al. 2007; Williams et al. 2009). Although such colors can be derived directly from the templates used for photometric redshift fitting, by definition these colors are confined to the range of colors spanned by the template set (which may be narrower than the intrinsic range of the galaxy population). Instead, we interpolate rest-frame U , V , and J fluxes directly from the observed photometry and photometric redshifts using the same method as Williams et al. (2009) but with the new H -band data included. This is accomplished using the InterRest utility (Taylor et al. 2009a), which in turn is an implementation of the method described by Rudnick et al. (2003). The reddest observed band in our data set is IRAC 4.5 μm , corresponding to rest-frame J at $z \sim 2.5$; reasonably robust fluxes can thus be interpolated up to approximately this redshift.

2.4. Completeness

In general, the mass completeness limit of a flux-limited galaxy sample depends strongly on color: since red galaxies have higher mass-to-light ratios, mass-limited red galaxy samples become incomplete at brighter magnitudes than for blue galaxies. Completeness limits derived for strongly heterogeneous (mixed red and blue) samples are therefore dominated by blue galaxies, and such samples can still exhibit serious incompleteness effects among massive red galaxies. Computing mass limits from red galaxies alone therefore provides a more conservative estimate of the overall sample completeness.

We derive mass completeness limits for the UDS sample by comparing the masses of red galaxies ($U - V_{\text{rest}} > 1.5$) to their observed K magnitudes. The 75% completeness limit is then defined as the mass at which about 25% of the galaxies in the sample fall below the adopted K flux limit. This is performed for the $1.5 < z_{\text{phot}} < 2.0$ redshift bin, thus ensuring that our analysis does not suffer from significant incompleteness effects up to $z = 2$. To ensure accurate size measurements, the size and surface density analysis is restricted to galaxies with $K_{\text{lim}} < 22.4$ (approximately 1 mag brighter than the formal 5σ survey limit; also used in Williams et al. 2009), corresponding to a mass limit of $\log M_* > 10.6$.

3. THE RELATION BETWEEN MASS, SIZE, AND STAR FORMATION

3.1. Mass–Size Relation

Our newly constructed sample allows us to study the mass–size relation and its evolution to $z = 2$. This relation, in three redshift bins from the UDS, is plotted in Figure 2. To supplement the higher-redshift data, the same relation from SDSS at $z \sim 0$ is also shown.

Two notable trends stand out: first, there is a correlation between radius and mass, whereby the most massive galaxies

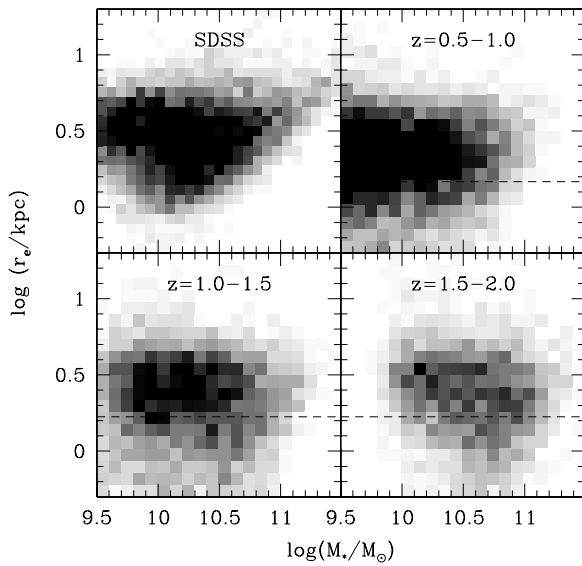


Figure 2. Size–mass relation for galaxies at $z \sim 0.06$ (SDSS; upper left) and three redshift ranges in the UKIDSS UDS. The grayscale denotes the number of points within each bin; dashed lines indicate the angular radii ($\theta \sim 0''.2$) below which individual size measurements have larger uncertainties. Massive, compact galaxies (i.e., those in the lower right-hand portion of each panel) are almost nonexistent at $z = 0$ but become progressively more common at higher redshifts. The radii of galaxies with $M > 10^{10.8} M_{\odot}$ evolve roughly as $r_e \sim (1+z)^{-0.89}$ (also see Table 2).

out to $z = 1.5$ have on average larger sizes than less massive galaxies; this effect is weaker or nonexistent at $z = 1.5\text{--}2$. A second and related point is that there are effectively no massive, compact galaxies ($M > 10^{11} M_{\odot}$, $r_e \lesssim 2$ kpc; in the lower right-hand region of the size–mass plot) at $z = 0$,

but at higher redshifts this area of parameter space becomes progressively more populated. This simply reflects the strong size evolution of massive galaxies found in several previous studies and introduced in Section 1.

3.2. Star Formation as a Function of Mass and Size

Kauffmann et al. (2003, 2006) and Franx et al. (2008) showed that the broad range in galaxy effective radii, at a given mass, is tightly correlated with sSFR out to $z = 2.5$. These authors concluded that sSFR is a tight function of stellar mass surface density (M_*/R^2) or velocity dispersion ($\sqrt{M_*/r_e}$; Franx et al. 2008). Put differently, these results imply that the size–mass relation is different for galaxies with different sSFRs.

Our sample is ideally suited to study this aspect at higher redshifts, as it covers an area ~ 18 times larger than that used by Franx et al. (2008). We show in Figure 3 how the sSFR depends on mass and size. It is clear that the dependence is very strong: at a given mass, galaxies with low sSFRs (binned and plotted as red/yellow squares in this figure) have small sizes, while those with large sizes have high sSFRs (green/blue squares). The effect is not only strong at very low redshift, but extends to the highest-redshift bins. At the same time, the sizes of galaxies with low sSFRs (red in the figure) are very small at high redshift, consistent with results obtained by others on smaller samples (Toft et al. 2007, 2009; van Dokkum et al. 2008; Franx et al. 2008).

Table 1 lists the best-fit slopes and normalizations of the *quiescent galaxy* size–mass relations seen in Figure 3. For this we defined “quiescent” as galaxies exhibiting $\text{sSFR} < 0.3/t_H$, where t_H is the age of the universe at each galaxy’s redshift, effectively picking out the red and yellow points in Figure 3 (see also Section 4 and the Appendix). In each redshift interval, the median log effective radius was calculated in mass bins of width

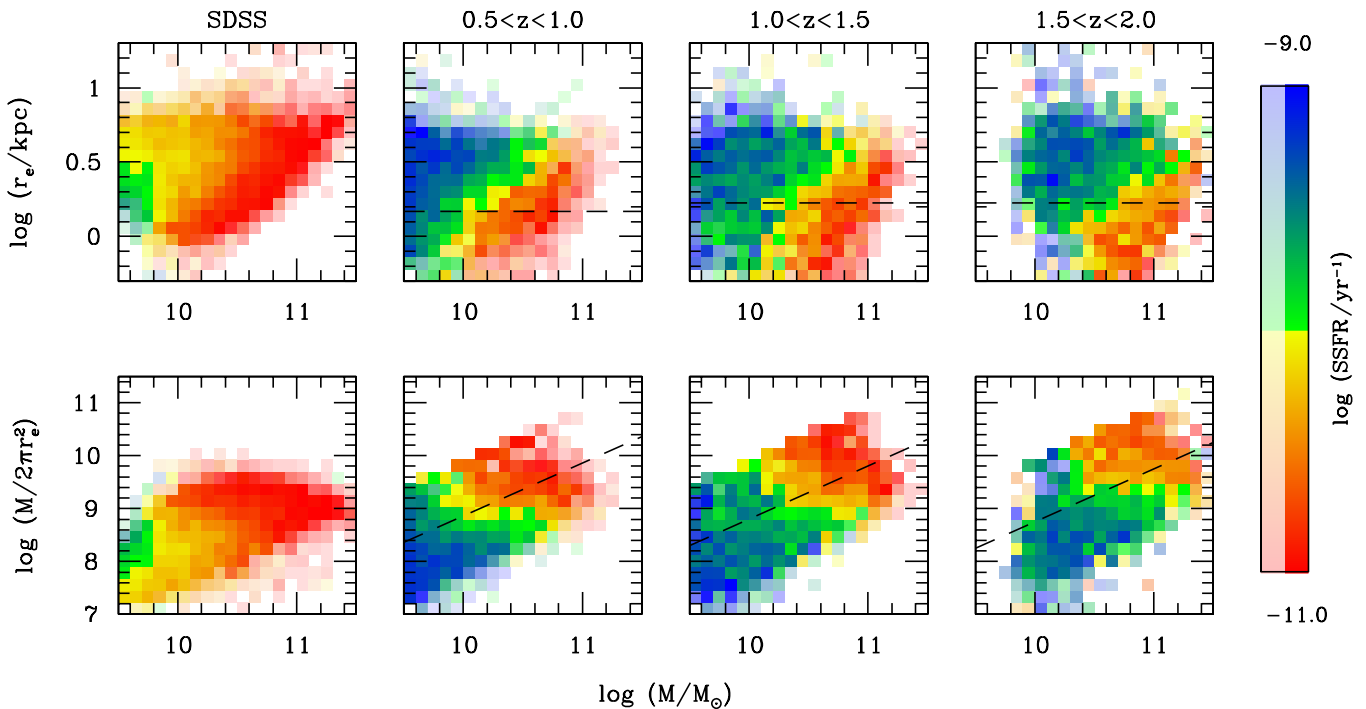


Figure 3. Top: size–mass relation in SDSS (left panel) and three UDS redshift bins: $z = 0.5\text{--}1.0$, $z = 1.0\text{--}1.5$, and $z = 1.5\text{--}2$ in the second, third, and fourth panels, respectively. Bottom: surface-density–mass relation in the same redshift bins. In all plots, the color denotes the mean sSFR of the underlying galaxies; “faded” bins contain two or fewer galaxies. Dashed lines indicate apparent effective radii of $0''.2$, below which (or above the corresponding surface density) individual galaxy size measurements have relatively large uncertainties (though the binned averages are more reliable). Strong evolution is evident in the mass–size and mass–surface density relations of low-sSFR galaxies, and the compact, dense galaxies which are clearly present in the early universe gradually vanish with decreasing redshift.

Table 1

Fits to the Quiescent Galaxy Size–Mass Correlations Shown in Figure 3

Redshift	A	b
SDSS	0.634 ± 0.004	0.41 ± 0.01
$0.5 < z < 1.0$	0.46 ± 0.02	0.54 ± 0.06
$1.0 < z < 1.5$	0.35 ± 0.01	0.56 ± 0.06
$1.5 < z < 2.0$	0.25 ± 0.01	0.50 ± 0.07

Notes. These fits only include quiescent galaxies ($sSFR < 0.3t_H$, where t_H is the age of the universe at each redshift (see the Appendix); red points in Figure 3). Note that there may be systematic offsets between the SDSS and high-redshift sizes and/or masses. Best-fit parameters are defined as $\log r_e = A + b(\log M/M_\odot - 11)$, so that 10^A is the typical radius of a $10^{11} M_\odot$ galaxy in kpc.

0.2 dex, only including galaxies above the mass completeness limit at each redshift, and a least-squares fit was performed to these median points. For convenience, the normalizations of the power-law fits in Table 1 are defined as the log effective radius of a typical galaxy with $M = 10^{11} M_\odot$. Uncertainties were computed using bootstrap resampling. Note that any comparisons between the mass–size relations seen in SDSS and UDS should be treated with caution, as systematic differences in the size and mass determinations between these two samples may exist. Nonetheless, strong evolution in the normalization of the size–mass relation is evident; the slope of the relation, however, does not significantly change between $z = 0.5$ and 2.

As the strong mass–size correlation of quiescent galaxies implies, sSFR does not depend strictly on size or mass alone, but rather on some combination of the two. The bottom panels of Figure 3 instead show how sSFRs depend on stellar mass surface density ($\Sigma_\star = M/2\pi r_e^2$) and mass. Galaxies with the highest surface densities have weak star formation, with very little dependence on mass. In addition, we can define a “threshold surface density” between quiescent and star-forming galaxies (similar to that defined by Franx et al. 2008) at each redshift; in Figure 3, the sharp color division (between green and yellow) at $\log sSFR = -10.0$ could be taken as a simple example of one such threshold. This clearly increases with increasing redshift. Note that this particular threshold depends only weakly on mass (i.e., is nearly horizontal in the Σ –mass plot), confirming that surface density is more fundamentally related to star formation activity in galaxies than mass (Franx et al. 2008).

Furthermore, this figure clearly shows at which epoch galaxies of a given size, mass, and density were forming stars: for example, galaxies with $M = 10^{11} M_\odot$ were generally star forming at $z \sim 2$ but by $z = 1.0$ – 1.5 most of their star formation activity had ceased. However, the most compact massive galaxies (the lower right-hand region of the radius–mass plot) are quiescent at all redshifts considered here, and must have been quenched at $z > 2$.

Most intriguingly, the compact quiescent galaxies visible at high redshift do not maintain their small sizes or high surface densities to lower redshifts; instead, the quiescent galaxies progressively evolve to larger radii and lower surface densities with decreasing redshift. This phenomenon is apparent from the UDS data alone in Figure 3, but is most starkly illustrated by the $z \sim 0$ SDSS panel where essentially no massive, compact galaxies are visible. This re-illustrates the phenomenon pointed out by van Dokkum et al. (2008), Trujillo et al. (2009), and Taylor et al. (2009b), but with multiple redshift bins the depletion of these galaxies is now easily seen. Since these galaxies are unlikely to be losing more than a small fraction of their mass (via mass loss from evolved stars; Damjanov et al.

2009), size evolution must be the primary driver behind their disappearance.

The trends shown in Figure 3 could, in principle, be affected by certain assumptions we have made. First, a minimum sSFR of 10^{-11} yr^{-1} has been imposed as a lower limit to what can be measured with SED fitting; however, varying this limit only serves to shift the apparent “quiescence threshold” in this figure, without affecting the overall trends. Again, the absolute radius, mass, and sSFR values may exhibit some systematic offsets between the SDSS and UDS samples due to different fitting and calculation methods, but the *relative* values within each frame (and between the three UDS redshift bins) are generally consistent. It is also possible that some degeneracies may exist between the mass and sSFR estimates used here since both stem from the same template fits (and hence are not entirely independent quantities). To test the robustness of these results, we reproduced Figure 3 using the SWIRE 24 μm data in this field as a fully independent sSFR diagnostic. A relation between the sSFR and $f_{24 \mu\text{m}}/f_K$ (with a minor correction using f_R/f_K to account for low-mass blue galaxies) is presented in Williams et al. (2009; the Appendix). Using the 24 μm data in place of the best-fit SED sSFR does not significantly change the results shown in Figure 3 (though it is somewhat noisier, due to the shallowness of the SWIRE 24 μm data).

4. THE STRUCTURAL EVOLUTION OF STAR-FORMING AND QUIESCENT GALAXIES

The strong size and surface density evolution of the “red and dead” galaxy population, and the apparent “disappearance” of the most compact objects, presents an intriguing puzzle for observers and theorists alike. In order to take full advantage of the unprecedented sample size of the UDS and provide constraints for present and future models, we now turn to quantifying these trends.

Figure 4 shows the sizes and surface densities of $M_\star > 10^{10.8} M_\odot$ galaxies as a function of redshift. This mass limit is equivalent (given the difference in IMF) to the limits employed by van Dokkum et al. (2008) and van der Wel et al. (2009). Quiescent galaxies (selected via the “quiescent red sequence” method described in the Appendix and by Williams et al. 2009) are shown in red and star-forming galaxies are shown in blue. van der Wel et al. (2009) note that any proposed models for the size evolution of quiescent galaxies (in particular those relying on dry mergers) are additionally constrained by the comoving mass and/or number densities of these galaxies as a function of redshift. The right-hand panel of this figure thus shows the number density evolution of quiescent galaxies with $\log(M_\star/M_\odot) > 10.8$; this was calculated at $z > 0.5$ with galaxy counts in three redshift bins from the UDS, and at $z \sim 0$ by integrating the SDSS Value Added Galaxy Catalog mass function tabulated by Yang et al. (2009). The plotted UDS number densities only include Poisson uncertainties; cosmic variance and selection effects have not been taken into account. Since the UDS sample is more than 99% complete at these somewhat higher masses, no correction to the best-fit number densities is necessary.

The trends seen in these three quantities are quite well fitted with power-law functions of the form $Y \sim (1+z)^\alpha$, where $\alpha = -1.09, 2.38, \text{ and } -1.0$ for $Y = r_e, \Sigma_\star, \text{ and } n$, respectively (best-fit α and normalization values are also listed in Table 2 for this and other samples). These fits were performed only to individual galaxies between $z = 0.5$ and 2.0, excluding the SDSS data and points that are major outliers in effective radius

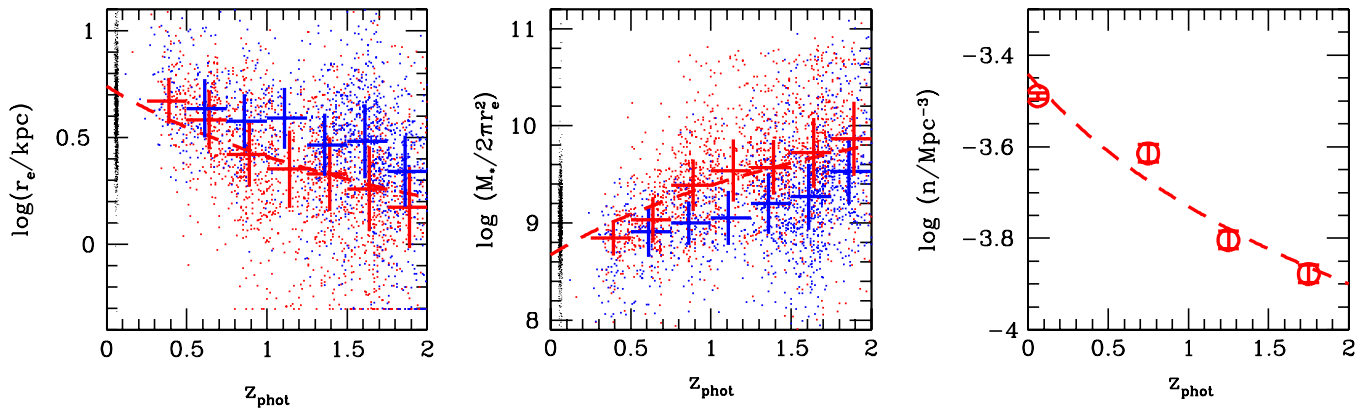


Figure 4. Left: evolution of $\log(M_*/M_\odot) > 10.8$ quiescent (red points) and star-forming (blue points) galaxy effective radii. Here “quiescent galaxies” are defined as those falling on the quiescent red sequence illustrated in Figure 6. The large blue and red crosses show the median radii of star-forming and quiescent galaxies, respectively, in bins of $\Delta z = 0.25$. The dashed line is a power-law (in $1+z$) fit to the small red points. Small black points near $z = 0.06$ are from the SDSS; note that these points were *not* included in the power-law fit. Center: same as the left panel, but for galaxy surface densities. Right: evolution of the massive quiescent galaxy number density with redshift. Error bars for the $z = 0.5$ – 2 points do not take cosmic variance or selection uncertainties into account; only Poisson errors are included. Here the $z \sim 0$ point is computed from the SDSS red galaxy mass function of Yang et al. (2009). The observed strong evolution since $z = 2$ in each of the three quantities (size, surface density, and comoving number density) is well described with a power law in $(1+z)^\alpha$, where $\alpha = -1.09, 2.37,$ and -1.0 , respectively. (A color version of this figure is available in the online journal.)

Table 2
Best-fit Power-law Parameters^a for the Structural Evolution of Massive Galaxies

Sample	α_r	b_r	α_Σ	b_Σ	α_n	b_n
All	-0.88 ± 0.06	0.73 ± 0.02	1.92 ± 0.11	7.90 ± 0.04
Quiescent red sequence	-1.09 ± 0.08	0.74 ± 0.03	2.37 ± 0.14	7.87 ± 0.05	-0.96 ± 0.13	-3.44 ± 0.07
Non-(quiescent RS)	-1.09 ± 0.08	0.88 ± 0.03	2.44 ± 0.15	7.52 ± 0.06
sSFR $< 0.3/t_H$	-1.17 ± 0.07	0.78 ± 0.02	2.52 ± 0.13	7.80 ± 0.04	-0.73 ± 0.14	-3.45 ± 0.08
sSFR $> 0.3/t_H$	-0.92 ± 0.09	0.85 ± 0.03	2.14 ± 0.18	7.57 ± 0.07
$(U - V) > 1.5$	-1.00 ± 0.06	0.75 ± 0.02	2.23 ± 0.12	7.83 ± 0.04	-0.47 ± 0.19	-3.45 ± 0.10
$(U - V) < 1.5$	-1.26 ± 0.19	0.98 ± 0.08	2.79 ± 0.40	7.30 ± 0.16

Notes. In all subsamples a mass cut of $\log(M_*/M_\odot) > 10.8$ has been imposed. The SDSS data were only included in the fit for α_n ; the α_r and α_Σ fits were based solely on UDS data.

^a Power-law parameters are defined such that $f(z) = b_f(1+z)^{\alpha_f}$, where f is r_e , Σ_* , or n ; uncertainties are estimated with bootstrap resampling.

Table 3
Size Evolution Power-law Fits in Different Mass Bins

$\log M_*/M_\odot$	All		Quiescent		Star Forming	
	α_r	b_r	α_r	b_r	α_r	b_r
10.6–10.8	-0.51 ± 0.07	0.51 ± 0.02	-0.75 ± 0.10	0.44 ± 0.03	-0.77 ± 0.08	0.70 ± 0.03
10.8–11.0	-0.81 ± 0.07	0.66 ± 0.03	-1.06 ± 0.11	0.66 ± 0.04	-1.10 ± 0.10	0.86 ± 0.04
> 11.0	-1.09 ± 0.09	0.87 ± 0.03	-1.30 ± 0.10	0.90 ± 0.03	-1.32 ± 0.15	1.03 ± 0.05

Notes. Power-law parameters α_r and b_r are defined such that $r_e(z) = b_r(1+z)^{\alpha_r}$. Quiescent and star-forming subsamples are selected via the “quiescent red sequence” method described in the Appendix.

($\log r_e > 1.1$ or $\log r_e < -0.25$). However, the SDSS data point was included in the fit to the number density evolution. For comparison, van der Wel et al. (2009) find that effective radii of early-type galaxies with Salpeter (1955) masses $> 10^{11} M_\odot$ (equivalent to our mass limit) are 0.54 ± 0.04 times smaller at $z = 1$ than $z = 0$ and 0.3 ± 0.1 times smaller at $z = 2$. In both size and surface density, the evolution they infer is somewhat slower than what we find; this might be a result of different sample selection methods. They also derive a comoving mass density equal to $35\% \pm 13\%$ of the local value at $z = 1$ and $10_{-6}^{+4}\%$ at $z = 2.4$, while our number density evolution is somewhat shallower than this (although roughly consistent between $z = 0$ and 1), implying significant mass growth in the existing quiescent galaxy population over these redshifts.

The above fits include galaxies spanning a somewhat wide range of masses ($\log M/M_\odot > 10.8$), but with this large sample it is possible to investigate the growth of galaxies as a function of stellar mass. Table 3 lists size evolution power-law indices (α_r) and normalizations (b_r) for these same quiescent and star-forming subsamples (as well as the total sample) in three narrower mass bins. A strong trend is immediately apparent: more massive galaxies undergo significantly faster size evolution with redshift. For the total sample α_r steepens from -0.52 to -1.09 between stellar masses of $10^{10.6}$ and $> 10^{11} M_\odot$, and from about -0.8 to -1.3 over the same mass interval for both the quiescent and star-forming subsamples. A similar trend was also noted by Franx et al. (2008). Although this could, in principle, be due to systematic galaxy mass

overestimates at high redshift, such offsets would need to be quite large and redshift dependent (e.g., ~ 0.2 – 0.3 dex too high at $z \sim 2$, but correct at $z \sim 0.5$). We therefore conclude that there is strong evidence for differential size evolution with mass.

As noted in the [Appendix](#), a number of other physically meaningful definitions of “quiescence” are possible and may be simpler to define within certain models. We thus repeated the power-law fits to other $\log M/M_\odot > 10.8$ quiescent galaxy samples defined through the other two selection methods described in the [Appendix](#), i.e., based on low best-fit sSFR ($< 0.3t_H$) and red rest-frame colors ($U - V_{\text{rest}} > 1.5$). For completeness, we performed the same fits to the size and surface density evolution of the complementary samples (star forming and blue), as well as all massive galaxies in this sample. Errors on the power-law slopes were computed using bootstrap resampling. The results of these fits are tabulated, along with the reference “quiescent red sequence” sample, in [Table 2](#). The sizes and surface densities of the different samples evolve at similar rates (differing by no more than 2σ for any two “equivalent” samples, e.g., low sSFR and quiescent red sequence). The observed structural evolution thus appears to be more or less independent of the exact technique used to select quiescent galaxies. Interestingly, massive galaxies overall exhibit slower evolution than either of the star-forming or “dead” subsamples; this is simply a consequence of the increasing fraction of massive quiescent galaxies at lower redshifts.

5. HOW UNIVERSAL IS THE STAR FORMATION GALAXY STRUCTURE CONNECTION?

From the preceding sections it is clear that star formation and galaxy structure are tightly coupled. While it was already established that such correlations exist ([Toft et al. 2007](#); [Franx et al. 2008](#)), the order-of-magnitude larger galaxy sample provided by the UDS allows us to not only observe and quantitatively measure said correlations, but also to investigate how uniformly the galaxy population at high redshift is described by them. In this final section, we present some alternate tests of the connection between structure and star formation, with the specific goal of qualitatively understanding the degree to which these relations are “universal.”

5.1. Average Spectral Energy Distributions

Average SEDs are an invaluable tool for ascertaining both the underlying spectral shapes of large galaxy samples and the scatter (or lack thereof) in their SEDs. To determine whether dense galaxies are universally quiescent, we separate all $z = 1$ – 2 , $K < 22.4$ UDS galaxies into four *surface density* bins and construct average rest-frame SEDs using their observed, de-redshifted photometric data points. [Figure 5](#) shows these photometric data (normalized at 8000 \AA) in each bin; median and 75% dispersion values of the individual galaxy points in bins of rest-frame wavelength are overplotted. To guide the eye, four Bruzual & Charlot (2003) stellar population models (from bottom to top, one single-burst model with age 1 Gyr and three constant star forming with increasing levels of dust obscuration) are also shown in each panel; note that these are *not* fits to the data.

This figure provides a nearly model-independent confirmation of the result shown in [Figure 3](#): namely, that the densest galaxies exhibit an average spectral shape that is well represented by an evolved stellar population, with remarkably low dispersion. Interestingly, there appears to be a smooth progres-

sion between average surface density and dust properties: galaxies with the lowest $\log \Sigma$ are typically blue and have low dust obscuration, but with increasing surface density the SEDs become dustier. It is especially notable that this does not appear to be caused by the addition of progressively more quiescent galaxies to the blue galaxy population; at least in the lowest two $\log \Sigma$ bins, the median SEDs are unambiguously within the “dusty” regime. Thus, it appears that there is not only an anticorrelation between sSFR and surface density, but also a positive correlation between *dust* and surface density for star-forming galaxies. However, since the sSFR is a mass-normalized quantity and the (qualitative) dust obscuration seen in [Figure 5](#) is not, we caution that this last point may be entirely due to more massive galaxies containing more total dust.

More importantly, the SED dispersion of the highest-density galaxies is at least a factor of 2 lower than for less-dense galaxies. This strongly implies that the highest-density galaxies are overwhelmingly represented by a single model with relatively few outliers; at lower surface densities, on the other hand, galaxies show larger dispersions in their spectra and thus span a range of spectral shapes. The comparatively low scatter in the high-density galaxies further reinforces the idea that they are by and large quiescent: if they instead were predominantly red due to dust obscuration, they would most likely exhibit large dispersions comparable to the SEDs in the lower-density bins. A quiescent galaxy model also provides a somewhat closer representation of the 4000 \AA break region than the $A_V = 3$ model, but the models underpredict the observed UV flux in these galaxies, indicating that there may be some contribution from very dusty starbursts or low levels of residual star formation in the “quiescent” galaxies.

5.2. Galaxy Structure in Color–Color Space

Up until now we have primarily investigated the star formation (and SED) properties of galaxies as a function of structural parameters. We now consider the converse question: what are the structural parameters of galaxies as a function of their star formation properties?

[Williams et al. \(2009\)](#) describe the use of the rest-frame $U - V$ versus $V - J$ (hereafter UVJ) diagram as a powerful diagnostic of both star formation activity and dust obscuration. [Figure 6](#) shows this diagram for all $z = 1$ – 2 galaxies in the UDS. In short, quiescent galaxies fall in a discrete clump in the upper left-hand region of this plot (above the dashed line), while star-forming galaxies form a “dust sequence” extending from the lower-left (blue) to upper-right (red) region. The utility of this plot as a star formation diagnostic was confirmed using stacked $24 \mu\text{m}$ data; a more thorough discussion is provided in the [Appendix](#).

In each panel of [Figure 6](#), galaxies have been binned and color-coded by their median: panel (a) sSFR, panel (b) mass, panel (c) effective radius, and panel (d) surface density. In the first panel, we confirm with our SED-based sSFR estimates what was previously shown by [Williams et al. \(2009\)](#) with $24 \mu\text{m}$ data—the “quiescent red sequence” (above the dashed diagonal line) is indeed overwhelmingly populated by quiescent galaxies, while red galaxies that do not lie on this sequence have significant star formation, and are thus dusty starbursts. Panels (b) and (c) illustrate how most quiescent galaxies have large masses and small effective radii, but some systematic variation is clearly present (due to the size–mass relation). However, in the final panel it is evident that quiescent galaxies almost uniformly exhibit high *surface densities*; there appears to be little variation in surface density with either mass

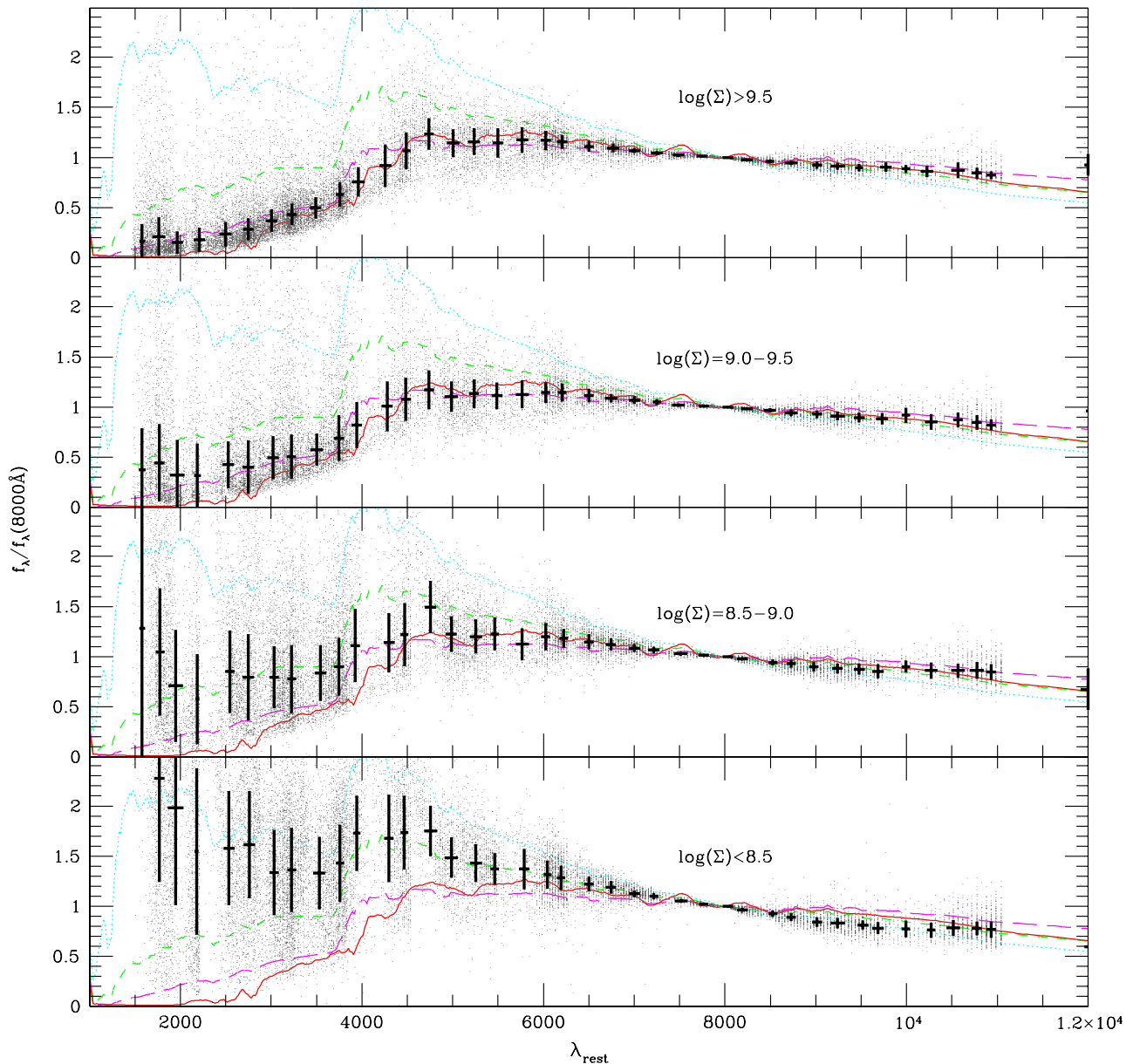


Figure 5. Average SEDs of all $K < 22.4$ galaxies between $z = 1$ and 2 in four stellar surface density bins. Small dots represent broadband flux measurements of individual galaxies, thick black bars denote the median and interquartile dispersion of the individual points, and overplotted lines show Bruzual & Charlot (2003) models of quiescent (1 Gyr age; solid lines) and star-forming galaxies with $A_V = 1$ (dotted), 2 (short dashed), and 3 (long dashed). The composite SED of the highest surface density galaxies is well represented by an old or a very dusty stellar population template.

(A color version of this figure is available in the online journal.)

or size along the quiescent red sequence. The converse also appears to hold true: the highest-density galaxies almost entirely fall within the “quiescent” region, confirming the result shown in Figure 5 (although some of the reddest star-forming galaxies exhibit densities approaching those of quiescent galaxies).

Though useful for illustrating the utility of the *UVJ* diagram, Figure 6 spans a fairly wide redshift range and may also contain systematic effects due to incompleteness at low masses. We therefore re-plot panels (c) and (d), the size and surface density as a function of color, in Figure 7 for four redshift bins. A mass limit of $\log M_* > 10.6$ (the 75% red-galaxy mass completeness limit at $z = 1.5$ – 2) is also imposed; thus, this figure is complete only up to $z = 2$ and we caution that the $z = 2$ – 2.5 bin likely suffers from some incompleteness effects as well as larger uncertainties in the masses and rest-frame colors.

The color–color plots shown in Figure 7 present a wealth of information about the structural evolution of massive galaxies and indeed provide a novel view of the results presented thus far. First, at all redshifts, quiescent galaxies (above the dashed line in each plot) exhibit small radii and large surface densities, though their surface densities are far more uniform than their sizes. However, while most massive compact galaxies are quiescent, the same is not always true for massive, high surface density galaxies: at $z \sim 2$, there are many dense, star-forming galaxies, but the number of such objects drops dramatically with decreasing redshift, suggesting that galaxies become quiescent at progressively lower surface densities with time. Even with this effect taken into account, it remains clear that the quiescent galaxy population undergoes dramatic structural changes from $z = 2$ to 0 , so another mechanism must be at work to bring about this transformation.

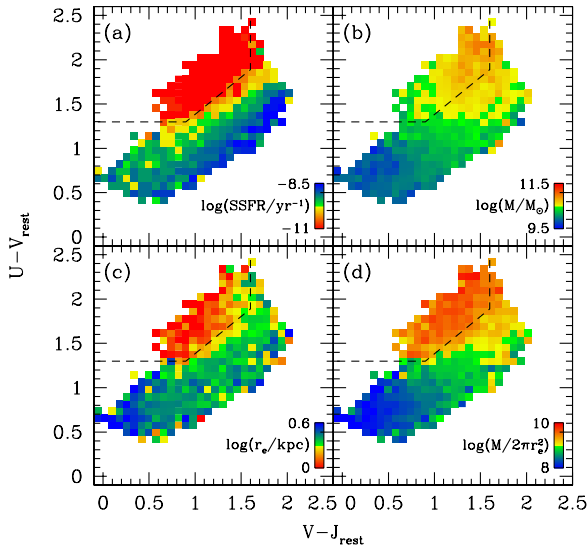


Figure 6. Rest-frame color–color plot for galaxies with $1.0 < z < 2.0$, binned and color coded by (a) log sSFR derived through SED fitting, (b) log(mass), (c) log(effective radius), and (d) log(surface density). The dashed line denotes the quiescent galaxy criterion of Williams et al. (2009), where galaxies above the diagonal belong to the “quiescent red sequence” and below the diagonal are star forming.

(A color version of this figure is available in the online journal.)

6. DISCUSSION

6.1. Comparison to Previous Work

By combining size measurements of a very large K -selected galaxy sample with SED fitting to determine SFRs and masses, we find that quiescent galaxies at all redshifts are far more compact than star-forming galaxies of comparable mass. Similar results have been found by other authors at high redshift (e.g., Daddi et al. 2005; Toft et al. 2007; Franx et al. 2008; Buitrago

et al. 2008; Cimatti et al. 2008), but with the larger sample size considered here, detailed investigations into the correlations between galaxy structure and star formation (and their evolution with redshift) are now possible. As shown in Figure 3, a well-defined mass–size relation for quiescent galaxies exists up to at least $z = 2$, but evolves to larger sizes with decreasing redshift. This figure also shows a clear anticorrelation between star formation activity and stellar mass surface density (nearly independent of mass), and an evolving surface density “threshold” above which galaxies are predominantly quiescent, confirming the findings of Franx et al. (2008).

The effective radii of $\log M/M_\odot > 10.8$ quiescent galaxies in this sample evolve as $\sim(1+z)^{-1.1}$ between $0.5 < z < 2$, with the power-law index varying only slightly depending on the exact definition of quiescence (see Table 2); this is in excellent agreement with the $(1+z)^{-1.22 \pm 0.15}$ “upsizing” observed by Franx et al. (2008) in a smaller sample from $z = 0-3$ and the factor 4.3 ± 0.7 size evolution since $z = 2.3$ seen by Buitrago et al. (2008). However, the slope of the size evolution varies strongly with mass such that the most massive galaxies show the fastest mass evolution (see Table 3). Trujillo et al. (2007) found evidence for similar mass-dependent evolution of “disk-like” galaxies between $0 < z < 1$; the sample presented here confirms that this result extends to higher redshifts and applies to the entire quiescent galaxy population.

The evolution in the UDS sample also agrees well with other previous studies specifically focusing on early-type galaxies; for example, van der Wel et al. (2009) find a factor of ~ 2 growth in size from $z = 1$ to the present and a factor of ~ 3 since $z = 2$, which agrees with the observed evolution in our “quiescent red sequence” sample. On the other hand, we find all galaxies above $\log M = 10.8$ exhibit size evolution with a power-law index of -0.88 ± 0.06 , slightly faster than the Franx et al. (2008) index of -0.71 ± 0.07 ; however, this may simply be due to the different redshift ranges considered. The total massive

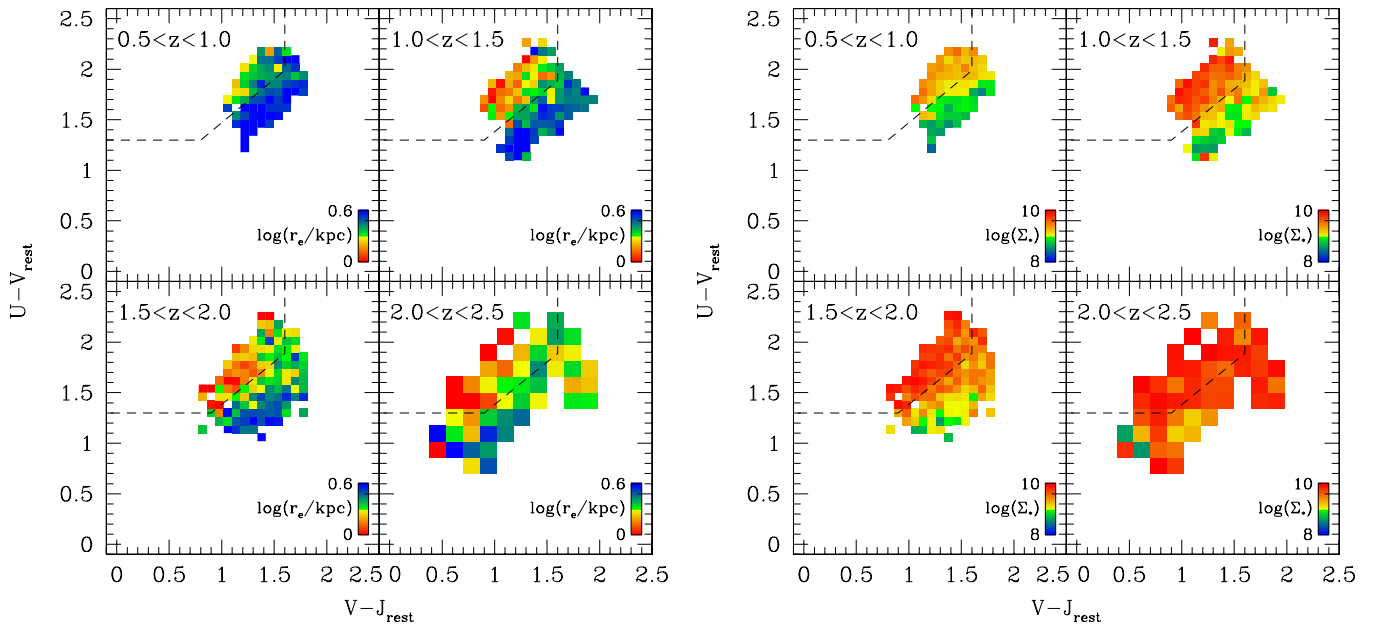


Figure 7. Left panel: rest-frame colors of galaxies in four redshift bins, color coded by median log effective radius. Quiescent galaxies lie above and to the left of the dashed line. Right panel: same as left, but with points color coded by log surface density (in $\log M_\odot/\text{kpc}^2$). A mass limit of $\log M_* > 10.6$ has been imposed; thus the $z = 2-2.5$ bin is likely incomplete. Quiescent galaxies have distinctly smaller sizes than star-forming galaxies at all redshifts; however, at $z > 1$ there appears to be a population of dense, star-forming galaxies.

(A color version of this figure is available in the online journal.)

galaxy sample grows more slowly in size than either quiescent or star-forming subsamples of similar mass, highlighting the increasing dominance of “dead” ellipticals over starbursts at lower redshifts.

In the highest-redshift bin, $z = 1.5\text{--}2$, we see a population of ultra-compact, high-density quiescent galaxies that are no longer present in the local universe or even (for the most part) at $z = 0.5\text{--}1$. Studies with higher-resolution data find that the typical sizes of $M > 10^{11} M_{\odot}$ quiescent galaxies at $z \sim 2.3$ are $r_e \sim 1$ kpc (van Dokkum et al. 2008), and at $z > 2$ no quiescent galaxies with $r_e > 2$ kpc are seen (Toft et al. 2007). Although 1 kpc is smaller than what we can confidently measure for individual galaxies, this size is consistent with our measurements. Figure 3 does, however, suggest the presence of quiescent galaxies at $1.5 < z < 2$ with somewhat extended radii ($r_e = 2\text{--}3$ kpc). A few such objects are also seen at similar redshifts (and with space-based imaging) by Damjanov et al. (2009); thus, the difference may simply be due to mild evolution of these galaxies from $z \sim 2.3$ to $z = 1.5$. Follow-up observations of candidate *extended* quiescent galaxies at $z \sim 2$ would confirm or rule out their existence, and perhaps shed some light on the mechanism behind the size evolution.

6.2. What Causes the Structural Evolution?

The presence of ultra-compact massive galaxies with extreme surface densities (and velocity dispersions; van Dokkum et al. 2009) at $z > 2$ is puzzling, since the prevalence of such objects is already diminished substantially by $z \sim 1.5$ (Franx et al. 2008; Cenarro & Trujillo 2009; Cappellari et al. 2009) and they effectively no longer exist at $z = 0$ (Trujillo et al. 2009; Taylor et al. 2009b). Major and minor mergers, in particular those involving only gas-poor galaxies (“dry mergers”), likely play a significant role in both the mass and size evolution of these objects (Khochfar & Silk 2008; Hopkins et al. 2009b; Feldmann et al. 2009). However, as suggested by van der Wel et al. (2009), other processes are also likely to be important, in particular, the quenching of progressively larger star-forming galaxies at lower redshift. Indeed, this may account for the seemingly incongruous result that the quiescent and star-forming samples each evolve faster than the overall galaxy population. In other words, if the compact, high surface density “tail” of the star-forming galaxy population is preferentially quenched at any given redshift, this will accelerate the apparent evolution of both subsamples.

The strong size growth of both massive star-forming and quiescent galaxies by itself suggests that major gas-poor (“dry”) mergers are not the only process driving massive galaxies’ strong structural evolution. Galaxies which are undergoing significant star formation must contain substantial amounts of gas, and therefore by definition cannot undergo dry mergers. However, the sizes and densities of massive star-forming galaxies are seen to evolve at a rate similar to the quiescent galaxies. It is therefore possible that at least one of the mechanisms acting on compact quiescent galaxies similarly affects star-forming galaxies.

Another proposed mechanism is adiabatic expansion, whereby mass loss from evolved stars decreases the potential well depth and therefore increases effective radii as galaxies age. As discussed by Damjanov et al. (2009), however, such a mechanism does not seem feasible because only a small fraction of the total mass is expected to be lost in passively evolving stellar populations between $z \sim 1.5$ and $z = 0$. The size growth may also be explained by many minor mergers or the accretion of relatively low-mass satellites. Naab et al. (2009) point out

that minor mergers are more efficient at increasing the radii of the primary galaxy than major mergers, per unit mass of the secondary galaxies. This scenario is also particularly attractive because it would depend only weakly (if at all) on whether or not the central galaxy is forming stars, and therefore could explain the size growth of both massive and quiescent galaxies. In a forthcoming paper, we will investigate the role of major and minor mergers on massive galaxy evolution (R. J. Williams et al. 2010, in preparation).

Although it is yet unclear what causes the observed size and surface density evolution of massive galaxies, the results presented herein illustrate how large, ground-based, near-IR surveys can provide large statistical samples, with sufficiently accurate size measurements, for comparison with the variety of theoretical models now under development. Upcoming instruments like VISTA and WFC3 will greatly enhance the volume and quality of available data; however, the proliferation of complementary observational results from existing surveys already presents an important challenge to, and constraints on, these models.

7. SUMMARY

By applying accurate size measurements and broadband SED fitting to the largest photometric sample of massive galaxies from $z = 0.5$ to 2 to date, we have investigated in detail the interplay between star formation, galaxy structure, and mass and its evolution with redshift. Our main conclusions are as follows.

1. Galaxies with low sSFRs follow a well-defined mass–size relation up to at least $z = 2$, and this relation moves to larger sizes at lower redshifts.
2. The anticorrelation between stellar mass surface density and star formation activity is much stronger than the size–sSFR relation; this confirms the result of Franx et al. (2008) that surface density and star formation are tightly connected at all redshifts.
3. Even with the far larger galaxy sample studied here, the densest, most massive galaxies seen at $z \sim 2$ have essentially disappeared by $z = 0.5\text{--}1$.
4. The sizes and surface densities of massive quiescent and star-forming galaxies evolve smoothly with time (following simple power-law behavior in $(1+z)$), with more massive galaxies exhibiting faster evolution.
5. Although galaxies with low surface densities exhibit a wide range of dust and star formation properties, at the highest surface densities their SEDs are well represented by a single quiescent galaxy model; thus, these “dense” galaxies comprise a relatively homogeneous population.

We thank Natascha Förster Schreiber for helpful discussions and the anonymous referee for suggestions that helped improve the manuscript. R.J.W. acknowledges support from the Netherlands Organization for Scientific Research (NWO) and the Leids Kerkhoven-Bosscha Fonds. R.F.Q. is supported by a NOVA postdoctoral fellowship and S.T. gratefully acknowledges support from the Lundbeck Foundation.

APPENDIX DEFINING QUIESCENCE

The primary goal of this work is to investigate the structural properties and evolution of quiescent galaxies, defined as those

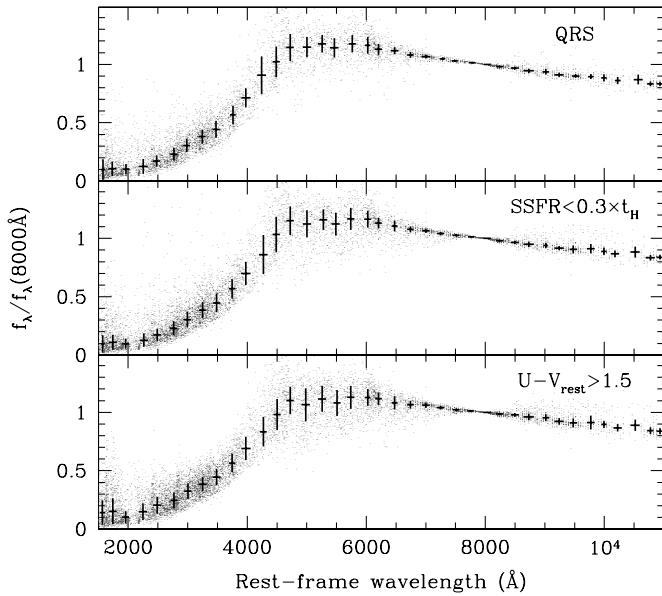


Figure 8. Average SEDs of $z = 1\text{--}2$ galaxies selected via the three methods described in the Appendix: the quiescent red sequence in the UVJ diagram (top panel); $s\text{SFR} < 0.3/t_H$ (center panel); and a simple $U - V > 1.5$ “red galaxy” cut (bottom panel). Black bars show the median and dispersion of the individual points in wavelength bins.

falling below some $s\text{SFR}$ threshold. In practice, there are a number of ways to define such a sample, particularly when only broadband photometric data are available. In this Appendix, we describe the primary selection technique employed for this analysis (the UVJ color–color selection described by Williams et al. 2009), as well as two alternate methods considered in Section 4. Average SEDs of the quiescent galaxies selected via these three techniques are shown in Figure 8. Note that these three average SEDs appear quite similar, suggesting that the three techniques are effective at selecting quiescent galaxies (though we caution that very dusty galaxies would not clearly stand out in these plots; see the models in Figure 5).

A.1. Quiescent Red Sequence

For the most part, galaxies which have ceased their star formation activity appear red due to their evolved stellar populations, and up to $z \sim 1.5$ or higher (depending on the data quality) form a well-defined “red sequence” when plotted in a color–magnitude diagram. However, at higher redshifts, progressively larger numbers of dusty starbursts are present, and these often exhibit optical colors which mimic “red and dead” galaxies, making the red sequence methods less reliable (especially with only broadband photometric data). As shown by Wuyts et al. (2007), incorporating rest-frame near-IR data into the analysis makes it possible to distinguish between dead and dusty galaxies. In particular, quiescent and star-forming galaxies occupy distinct regions of the rest-frame $U - V$ versus $V - J$ (UVJ) color space; with the UKIDSS UDS and overlapping data, Williams et al. (2009) found that a “quiescent red sequence” is clearly visible (and distinct from dusty star-forming galaxies) in the UVJ distribution up to $z = 2$ and criteria based on these colors provide an effective physical basis for separating quiescent from star-forming galaxies.

Figure 6 (left) shows the UVJ diagram for all galaxies between $1.0 < z < 2.0$ in the UDS with $K < 22.4$. The quiescent galaxy selection criterion defined in Williams et al. (2009) is shown as

a dashed line, where quiescent galaxies lie above and to the left of the line and star-forming galaxies are below. For reference, the criterion at $z = 1\text{--}2$ is

$$(U - V) > 0.88 \times (V - J) + 0.49. \quad (\text{A1})$$

At lower redshifts the criterion changes slightly, shifting upward by 0.1 dex (i.e., the 0.49 becomes 0.59). Additional constraints of $U - V > 1.3$ and $V - J < 1.6$ are imposed to prevent too many star-forming galaxies from scattering into the selection region.

We note that some of the galaxies defined via this method as “passive” may nonetheless still have emission in the mid-IR from dusty star formation or active galactic nuclei. When we compare this technique to deep $24 \mu\text{m}$ imaging in the Chandra Deep Field-South, we find that 4 out of 29 “quiescent red sequence” galaxies at $z = 2$ have significant $24 \mu\text{m}$ emission. Hence, this classification is not a guarantee that a given galaxy has no star formation. On average, however, as shown by Williams et al. (2009) for this field, the $24 \mu\text{m}$ emission is very low for these galaxies.

This empirical “quiescent red sequence” method is preferred to, e.g., SED fitting because photometric redshifts (as well as interpolated rest-frame colors based on these redshifts and observed fluxes) are typically the best-constrained parameter in broadband SED fitting. By providing a directly empirical criterion, the rest-frame color separation is also less subject to template-dependent systematics that may affect SED-based $s\text{SFR}$ s. We therefore adopt this color–color cut as our primary method for selecting quiescent galaxy samples.

A.2. Evolving $s\text{SFR}$ Cut

Since the UVJ technique is relatively new and some theoretical models may better predict SFR s, we consider a sample (listed as $s\text{SFR} < 0.3/t_H$ in Table 2) based on an evolving cut in galaxy $s\text{SFR}$ s. In this case, quiescent galaxies are defined as those exhibiting $s\text{SFR}$ s less than $0.3/t_H(z_i)$, where $t_H(z_i)$ is the age of the universe for each galaxy at redshift z_i , analogous to the quiescent galaxy definitions employed by Franx et al. (2008) and Fontana et al. (2009). The factor 0.3 is somewhat arbitrary, but is comparable to the $s\text{SFR}$ s of red sequence galaxies in our SDSS subsample.

A.3. Red Galaxies

Finally, one of the simplest criteria that can be defined is a single rest-frame color cut, i.e., assuming that all galaxies redder than a certain value are quiescent. As noted before, this method is somewhat flawed because sufficiently dusty starburst galaxies can mimic the colors of truly “red and dead” galaxies. Nonetheless, for completeness we construct a third sample with rest-frame $U - V > 1.5$ irrespective of $s\text{SFR}$.

REFERENCES

- Bell, E. F., et al. 2006, *ApJ*, 640, 241
 Bertin, E., & Arnouts, S. 1996, *A&AS*, 117, 393
 Bezanson, R., van Dokkum, P. G., Tal, T., Marchesini, D., Kriek, M., Franx, M., & Coppi, P. 2009, *ApJ*, 697, 1290
 Brammer, G. B., van Dokkum, P. G., & Coppi, P. 2008, *ApJ*, 686, 1503
 Bruzual, G., & Charlot, S. 2003, *MNRAS*, 344, 1000
 Buitrago, F., Trujillo, I., Conselice, C. J., Bouwens, R. J., Dickinson, M., & Yan, H. 2008, *ApJ*, 687, L61
 Bundy, K., et al. 2009, *ApJ*, 697, 1369
 Cappellari, M., et al. 2009, *ApJ*, 704, L34
 Cenarro, A. J., & Trujillo, I. 2009, *ApJ*, 696, L43

- Cimatti, A., et al. 2008, *A&A*, 482, 21
- Daddi, E., et al. 2005, *ApJ*, 626, 680
- Damjanov, I., et al. 2009, *ApJ*, 695, 101
- de Ravel, L., et al. 2009, *A&A*, 498, 379
- Feldmann, R., Carollo, C. M., Mayer, L., Renzini, A., Lake, G., Quinn, T., Stinson, G. S., & Yepes, G. 2009, *ApJ*, 709, 218
- Fontana, A., et al. 2009, *A&A*, 501, 15
- Förster Schreiber, N. M., et al. 2004, *ApJ*, 616, 40
- Franx, M., van Dokkum, P. G., Förster Schreiber, N. M., Wuyts, S., Labbé, I., & Toft, S. 2008, *ApJ*, 688, 770
- Hopkins, P. F., Bundy, K., Murray, N., Quataert, E., Lauer, T., & Ma, C.-P. 2009a, *MNRAS*, 398, 898
- Hopkins, P. F., Hernquist, L., Cox, T. J., Keres, D., & Wuyts, S. 2009b, *ApJ*, 691, 1424
- Joung, M. R., Cen, R., & Bryan, G. L. 2009, *ApJ*, 692, L1
- Kauffmann, G., et al. 2003, *MNRAS*, 341, 54
- Kauffmann, G., et al. 2006, *MNRAS*, 367, 1394
- Khochfar, S., & Silk, J. 2006, *ApJ*, 648, L21
- Khochfar, S., & Silk, J. 2009, *MNRAS*, 397, 506
- Kriek, M., van der Wel, A., van Dokkum, P. G., Franx, M., & Illingworth, G. D. 2008a, *ApJ*, 682, 896
- Kriek, M., van Dokkum, P. G., Labbé, I., Franx, M., Illingworth, G. D., Marchesini, D., & Quadri, R. F. 2009, *ApJ*, 700, 221
- Kriek, M., et al. 2006, *ApJ*, 649, L71
- Kriek, M., et al. 2008b, *ApJ*, 677, 219
- Kron, R. 1980, *ApJ*, 43, 305
- Kroupa, P. 2001, *MNRAS*, 322, 231
- Labbé, I., et al. 2005, *ApJ*, 624, L81
- Lawrence, A., et al. 2007, *MNRAS*, 379, 1599
- Lonsdale, C. J., et al. 2003, *PASP*, 115, 897
- Maier, C., et al. 2009, *ApJ*, 694, 1099
- Maraston, C. 2005, *MNRAS*, 362, 799
- Marchesini, D., et al. 2007, *ApJ*, 656, 42
- McCarthy, P. J., et al. 2004, *ApJ*, 614, L9
- Naab, T., Johansson, P. H., & Ostriker, J. P. 2009, *ApJ*, 699, L178
- Peng, C. Y., Ho, L. C., Impey, C. D., & Rix, H.-W. 2002, *AJ*, 124, 266
- Rudnick, G., et al. 2003, *ApJ*, 599, 847
- Rudnick, G., et al. 2006, *ApJ*, 650, 624
- Salpeter, E. E. 1955, *ApJ*, 121, 161
- Sekiguchi, K., et al. 2004, *BAAS*, 36, 1478
- Sérsic, J. L. 1968, *Atlas de Galaxias Australes* (Cordoba: Observatorio Astronómico)
- Stutz, A. M., Papovich, C., & Eisenstein, D. J. 2008, *ApJ*, 677, 828
- Taylor, E. N., et al. 2009a, *ApJ*, 694, 1171
- Taylor, E. N., et al. 2009b, *ApJ*, submitted (arXiv:0907.4766)
- Toft, S., et al. 2007, *ApJ*, 671, 285
- Toft, S., et al. 2009, *ApJ*, 705, 255
- Trujillo, I., Cenarro, A. J., de Lorenzo-Cáceres, A., Vazdekis, A., de la Rosa, I. G., & Cava, A. 2009, *ApJ*, 692, L118
- Trujillo, I., Conselice, C. J., Bundy, K., Cooper, M. C., Eisenhardt, P., & Ellis, R. S. 2007, *MNRAS*, 382, 109
- Trujillo, I., et al. 2006a, *ApJ*, 650, 18
- Trujillo, I., et al. 2006b, *MNRAS*, 373, L36
- van der Wel, A., Bell, E. F., van den Bosch, F. C., Gallazzi, A., & Rix, H.-W. 2009, *ApJ*, 698, 1232
- van der Wel, A., Holden, B. P., Zirm, A. W., Franx, M., Rettura, A., Illingworth, G. D., & Ford, H. C. 2008, *ApJ*, 688, 48
- van Dokkum, P. G., Kriek, M., & Franx, M. 2009, *Nature*, 460, 717
- van Dokkum, P. G., et al. 2008, *ApJ*, 677, L5
- van Dokkum, P. G., et al. 2010, *ApJ*, 709, 1018
- Warren, S. J., et al. 2007, *MNRAS*, 375, 213
- Williams, R. J., Quadri, R. F., Franx, M., van Dokkum, P., & Labbé, I. 2009, *ApJ*, 691, 1879
- Wuyts, S., et al. 2007, *ApJ*, 655, 51
- Yang, X., Mo, H. J., & van den Bosch, F. C. 2009, *ApJ*, 695, 900
- Zirm, A. W., et al. 2007, *ApJ*, 656, 66